A 3D voxel-based mesostructure generator for finite element modelling of tow-based discontinuous composites

(article starts on next page)

A 3D voxel-based mesostructure generator for finite element modelling of tow-based discontinuous composites

Luis Gulfo [a,b], Olle Haglund Nilsson [a], Jacob Sjöberg [a], Ioannis Katsivalis [a,b], Leif E. Asp [a,b], Martin Fagerström [a,b,*]

[a] *Department of Industrial and Materials Science, Chalmers University of Technology, Gothenburg, SE 41296, Sweden*
[b] *TechForH2 Excellence Centre, Chalmers University of Technology, Gothenburg, Sweden*

ARTICLE INFO

ABSTRACT

Tow-based discontinuous composites manufactured with ultra-thin tapes display high stiffness, strength, and in-plane isotropy, thus competing with composite laminates. Their complex 3D microstructure affects the mechanical response, in turn demanding 3D generators that capture the tape waviness, resin pockets, and thickness and fibre content variations. The present work proposes an automated numerical framework combining a 3D voxel-based mesostructure generator with finite element models. A modified 3D random sequential absorption technique is developed with bin-guided allocation, draping, and thickness control. A statistical study is used to size the statistical volume elements and predict the elastic properties of thick, thin, and ultra-thin tow-based discontinuous composites. The results are compared with the experimental values from the literature. Despite uncertainties in physical tape properties, the resulting stiffnesses are predicted with good accuracy.

1. Introduction

In high-performance applications, structures need to comply with strict requirements in terms of stiffness and strength, while being lightweight [1]. Recently, ultra-thin Tow-Based Discontinuous Composites (TBDCs) have shown promising stiffness and strength [2,3], which are superior to conventional Sheet Moulding Compounds (SMCs) [4] and similar to those of continuous fibre-reinforced composites [5]. Randomly-oriented TBDCs are manufactured by chopping UD prepreg tapes to specific dimensions, depositing them in random positions and in-plane orientations, and using compression moulding [6]. Thus, TBDCs are relatively easier to fabricate at low costs, as they use chopped UD prepreg and random deposition instead of controlled placement. SMCs differ from TBDCs as they are not based on UD tapes cut to specific design dimensions, but instead are based on sheets manufactured by chopping fibre bundles that are randomly dispensed onto a matrix [7], thus resulting in different microstructures and mechanical behaviour.

In contrast to thick TBDCs with tow thicknesses of 150–200 μm, ultra-thin TBDCs are manufactured using spread tow tapes, with a tow thickness down to 20 μm [3]. In this way, ultra-thin TBDCs

utilise the thin-ply effect to increase the in-situ strength by constraining matrix cracking [8,9]. Thus, ultra-thin TBDCs can compete with continuous fibre-reinforced composites in terms of manufacturability and mechanical properties, while having the benefit of an in-plane isotropy.

However, for structural applications there is a lack of numerical models for TBDCs due to their complex microstructure, random nature, and scatter in mechanical properties [10]. Several challenges result from the variability of the tape orientation, tape waviness induced by draping (i.e. bending of a tape over another), presence of resin pockets, varying fibre volume fraction, and uneven plate thickness [3,11]. It has been shown that tape waviness and weak spots with a low number of tapes affect both stiffness and strength, an effect which cannot be captured by 2D models as they do not include the out-of-plane orientations. For instance, it has been reported that 3D features like waviness cause stiffness reductions of 25% [11]. Therefore, there is a strong interest in the development of 3D computational models of TBDCs.

Equivalent Laminates (ELs) and 3D modelling approaches have been studied in the literature. Feraboli et al. [12] proposed a stochastic laminate analogy, which randomly generates the areas and orientations
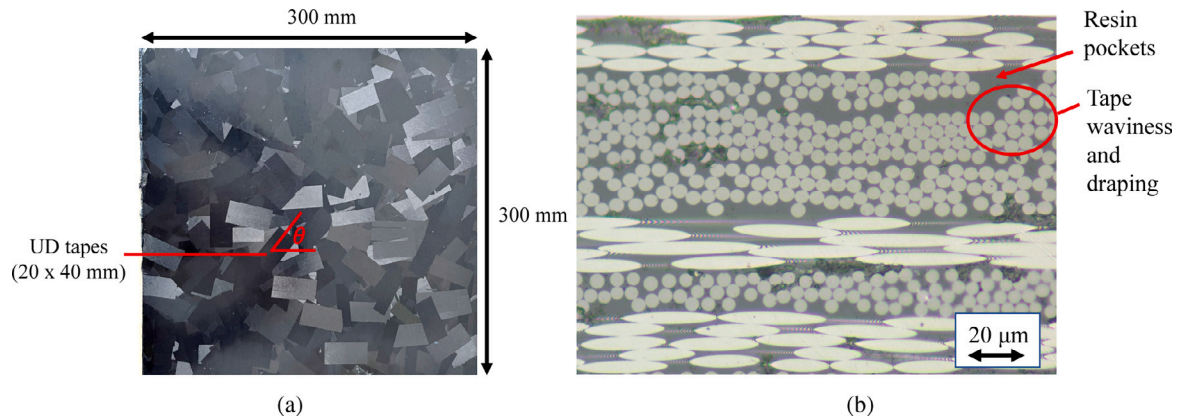

Fig. 1. Characteristics of the ultra-thin TBDC. (a) Top view of the plate with randomly oriented UD tapes, (b) Microscopic image of the transverse section showing tape draping, waviness and resin pockets.

for 2D tapes. Then, classical laminated theory is used to predict the mechanical properties. Although randomly generated, the tape dimensions and layup are not explicitly modelled. Selezneva et al. [13] developed a 2D random tape placement methodology that allows tape overlapping in the discretised domain, which are converted into a local panel density with a specific layup. However, the model does not take into account tape waviness and interactions, aspects required for more detailed modelling of damage mechanisms. Li and Pimenta [14] proposed a multi-scale approach that uses a shear-lag model to describe the interaction between tows and an isotropic EL at the macroscale.

More complex approaches have aimed to couple 3D microstructure generators with analytical methods. Ko et al. [15] proposed an extension of the laminate analogy by Feraboli et al. [12], using a platelet distribution algorithm to capture a spatial variation. However, the tapes remain flat and the thickness adjustment removes the thickness variations. Alves and Pimenta [11] developed a microstructure generator coupled with an analytical homogenisation. They used a so-called 3D Random Sequential Adsorption (RSA) method, in which each tape is sequentially generated at a random position and orientation, and added to a deposition domain to model the material. The varying tape orientations were then accounted for when averaging the stiffness properties assuming an iso-strain condition [11]. The previous models do not, however, incorporate resin pockets induced by draping at the end of the tapes. Instead, they include resin layers between the tapes, a feature that is not observed in experimental images [14]. Alves et al. [16] found that both deterministic and stochastic FE models of ELs tend to show over-predictions of the response due to lack of resin pockets, especially for strength, with errors greater than 20%.

Another approach to model TBDCs uses mean-field homogenisation with Fibre Orientation Distributions (FODs) extracted from process simulations or CT scans [17]. The former have been mainly studied for material systems of SMCs, i.e. with dispersed or bundled fibres. However, limited research has been conducted on tow-based architectures with tow-to-tow and tow-to-matrix (resin pockets) interfaces [18]. For instance, FOD prediction models used by software as Moldflow and Moldex3D are phenomenological, which require calibration for specific materials and regimes (i.e. diluted, semi-diluted or concentrated suspensions, closer to SMCs than to TBDC mesostructures) [19]. Alves et al. [16] showed that Moldex3D captured the global orientation average of a TBDC specimen, but was not able to reproduce local tow orientation variability at characteristic length-scales inside the specimen. Their model was calibrated with an SMC and then applied to a TBDC. Thus, using FODs from CT scans or calibrated process modelling is costly, limiting these approaches to existing materials and making them unsuitable for material optimisation.

Finally, fully 3D models for TBDCs have been explored by a few authors, either by modelling the explicit geometry or by using a voxel

model. Krishna Mohan et al. [20] proposed a 3D-RSA using cuboid inclusions to generate representative volume elements. However, the model neglects the tape waviness and applies to low tape volume fractions (around 22% or less). Also, no comparison with experimental data was provided. Shah et al. [21] used an embedded element technique, where tapes are shell elements embedded in a 3D matrix. To avoid tape interceptions, the representative volume element is divided into layers, and the tape waviness is constrained by a spline inside each layer. A tape volume fraction of up to 65% was studied, still below those of high-performance TBDCs. Recently, Ryatt and Ramulu [22,23] developed a 3D-RSA algorithm with tape draping, enabling a close tape interaction. The voxel model allows to control the local height of the tapes to overlay one tape on top of the other. During this procedure, resin pockets are introduced, a feature also observed in practice. This method can generate realistically high tape volume fractions (higher than 90%). The stiffness predictions showed good agreement with the experimental data (an error of around 4%), but validation was limited to cases with relatively thick tapes (0.127 mm).

It is evident that limited research has been conducted on numerical methods that capture the 3D microstructural variability found in TBDCs, especially considering waviness, random stacking with draping, high tape volume fractions, and resin pockets. Moreover, the tape thickness greatly influences the microstructure, for instance being more structured and less wavy when the tapes are thinner [3,6]. Thus, there is a lack of studies addressing the wide range of microstructures down to ultra-thin TBDCs.

The aim of this paper is twofold: (1) to develop and implement a numerical framework for the generation of 3D voxel-based mesostructures of thick, thin, and ultra-thin TBDCs; (2) to integrate voxel-based mesostructures in FE simulations, showcased by the computational homogenisation of elastic properties. This is accomplished through four main contributions. First, a modified 3D-RSA method with tape draping is developed in combination with generation strategies to control the spatial variations. In this respect, the method can be seen as an extension of the approaches presented in [15,21,22], where the differences are explained in Section 3. RSA methods have proven the potential to replicate geometrically the spatial variability found in TBDCs [11,24], which motivates the interest in extending such methods and their use over costly characterisations derived from CT scans or calibrated process simulations. Second, experimental data of an ultra-thin TBDC are analysed to extract modelling guidelines. Third, the generator is coupled with 3D FE simulations, through which a detailed statistical analysis is carried out to size the Statistical Volume Elements (SVEs) for the prediction of elastic properties. Compared to other studies, confidence intervals are provided not only for the tensile modulus but also for the shear modulus. Fourth, the predictions are compared with experimental data from the literature for the tensile stiffness of three

Table 1
TBDC plate properties for the three case studies.

Property	Units	Thick	Thin	Ultra-thin
t_p	mm	2.106	2.444	1.176
V_f^p	%	53.50 ± 5.39	57.85 ± 3.84	62.69 ± 5.69
E	GPa	39.66 ± 5.06	43.41 ± 4.14	69.9 ± 3.2
v_{xy}	–	–	–	0.363 ± 0.043
Reference		[6]	[6]	[2]

Table 2
UD tape properties for the three case studies.

Property	Units	Thick	Thin	Ultra-thin
t_t	mm	0.285	0.164	0.0214
l_t	mm	50	50	40
w_t	mm	8	8	20
V_f^t	%	57	57	62.69 ± 5.69[a]
E_1	GPa	121[b]	131[b]	197 ± 5[c]
$E_2 = E_3$	GPa	9	9	8.11 ± 0.05
$G_{12} = G_{13}$	GPa	5.6	5.6	2.98
G_{23}[d]	GPa	3.2143	3.2143	2.89
$v_{12} = v_{13}$	–	0.34	0.34	0.35 ± 0.03
v_{23}[e]	–	0.4	0.4	0.4
Reference		[14]	[14]	[2]

[a] Assumed equal to V_f^p since the tape volume fraction is significantly high, 99.5% (Section 2.2).
[b] Scaled from values of uni-axial tensile tests (116 GPa at $V_f^t = 51.3\%$) on HexPly-M77 to V_f^p [14].
[c] Scaled from experiments (172 ± 5 GPa at 54.7%) to V_f^p.
[d] $G_{23} = E_2/2(1 + v_{23})$.
[e] Assumed.

case studies comprising thick, thin, and ultra-thin TBDCs. Additionally, a comparison with predictions by ELs is included. It is highlighted that a comprehensive study of voxel-based 3D-RSA methods applied to different types of TBDCs as presented here has not been covered in the existing literature.

The organisation of the paper is as follows. Section 2 provides a description of the material, the case studies, and experimental results. Section 3 explains the voxel-based mesostructure generator. Section 4 demonstrates the application of the generator in FE simulations and computational homogenisation. Then, Section 5 presents the results and their discussion. Finally, conclusions are drawn in Section 6.

2. Materials

2.1. Case studies

To produce TBDCs, UD tapes are deposited at random angles and consolidated (Fig. 1(a)). The microstructure and properties depend on the tapes and the consolidation, which produce resin pockets and tape waviness/draping (Fig. 1(b)). A factor that significantly influences these features is the geometry of the UD tapes, with thickness to length ratio of the tapes being the dominating one. The modelling framework presented in Section 3 aims to cover thicknesses (assuming similar tape lengths) ranging from thick (0.285 mm) to ultra-thin (0.0214 mm). Therefore, three case studies are considered as benchmarks, including thick, thin and ultra-thin tapes. Thick and thin case studies are taken from [6], and the ultra-thin case from [2]. The material data are summarised in Tables 1 and 2. For the plate, properties include the thickness t_p, the fibre volume fraction V_f^p, the in-plane Young's modulus E, and the in-plane Poisson's ratio v_{xy}. The tape properties include the thickness t_t, length l_t, width w_t, fibre volume fraction V_f^t, and the elastic properties.

2.2. Experimental observations of the ultra-thin TBDC

This section complements the study recently conducted by Katsivalis et al. [2], and extracts modelling guidelines from the analysis of samples from that study. Plates with a size of 300 × 300 mm were manufactured using 20 × 40 mm ($w_t \times l_t$) tapes with a cured tape thickness of 0.0214 mm (Fig. 1(a)).

The fibre content in the ultra-thin TBDC was determined for five samples by matrix digestion using nitric acid (ASTM D3171 [25]). The ultra-thin TBDC has a global fibre volume fraction of 62.69 ± 5.69%. The measured stiffness and Poisson's ratio of the plate are 69.9 ± 3.2 GPa and 0.363 ± 0.043, respectively.

Seven microscopic images of the ultra-thin TBDC were also taken (e.g. Fig. 1(b)) to independently estimate the global fibre volume fractions of the plate. The microscopic images were converted into binary images (black and white) for the analysis, using Otsu's method [26] to separate fibres from the matrix, and using a binarisation threshold of 0.25 to separate voids from the other phases.

The percentage of voids obtained is less than 0.02%, which is very low, and justifies neglecting voids in the virtual mesostructure generator. On the other hand, the percentage of resin pockets has an estimated value of 0.5% (99.5% tape volume fraction) for ultra-thin TBDCs, which is lower than in thicker TBDCs (e.g. mean predicted and

experimental values between 2.5 and 4.9% were reported in [27]). These values should guide the choice of the draping ratio and voxel aspect ratio, as they affect the resin content. The average fibre and matrix area fractions of all the images are 65.0 ± 2.2% and 35.0 ± 2.2%, respectively. Thus, slightly higher than what was measured from the matrix digestion, which points out a possible source of uncertainty. Local variations in thickness and fibre content in the tapes were also observed, which may be attributed to compaction effects.

Finally, measurements of the thickness of the ultra-thin TBDC plate were collected. The mean value, the standard deviation, and the CoV are 1.176 mm, 0.087 mm, and 0.074 (7.4%), respectively. The latter are quite low, as expected for ultra-thin TBDCs, since the microstructure is less wavy and more regular (Fig. 1(b)) compared to thicker TBDCs, where values of the CoV around 0.22 (22%) have been reported [15].

3. Modelling TBDCs with voxel-based 3D mesostructure generator

This section presents the numerical framework (Fig. 2). The modified 3D-RSA technique is used to generate a 3D mesostructure in MATLAB [28], based on the tape voxelisation procedure, the sizing of the deposition domain, and deposition strategies. These are explained in the following.

It is highlighted that the proposed generator is robust enough to model full 3D TBDC plates, enabling different applications (Section 5.4). Fig. 2 shows the integration in the prediction of homogenised elastic properties, as covered in Section 4, using SVEs extracted from the plates. Due to the random geometry of TBDCs, and its impact on the scattering of mechanical properties, the framework incorporates a statistical analysis of N random independent realisations, which makes it possible to quantify variations. The SVE is used to build a 3D voxel-based FE model and homogenise the elastic properties. This contrasts with the modelling of conventional continuous fibre composites, where the idealisation of the geometry is acceptable.

3.1. Tape voxelisation procedure

To voxelise the tape thickness t_t, the number of voxels through the thickness $N_t^{vox,h}$ is set. For the voxelisation of the tape length l_t and width w_t, the aspect ratios of the cuboid voxel in the length and width directions are defined as the ratio between the voxel length and thickness ($R_{vox,l}$), and as the ratio between the voxel width and thickness ($R_{vox,w}$), respectively. Typically $R_{vox,l} = R_{vox,w} = R_{vox}$. Then,
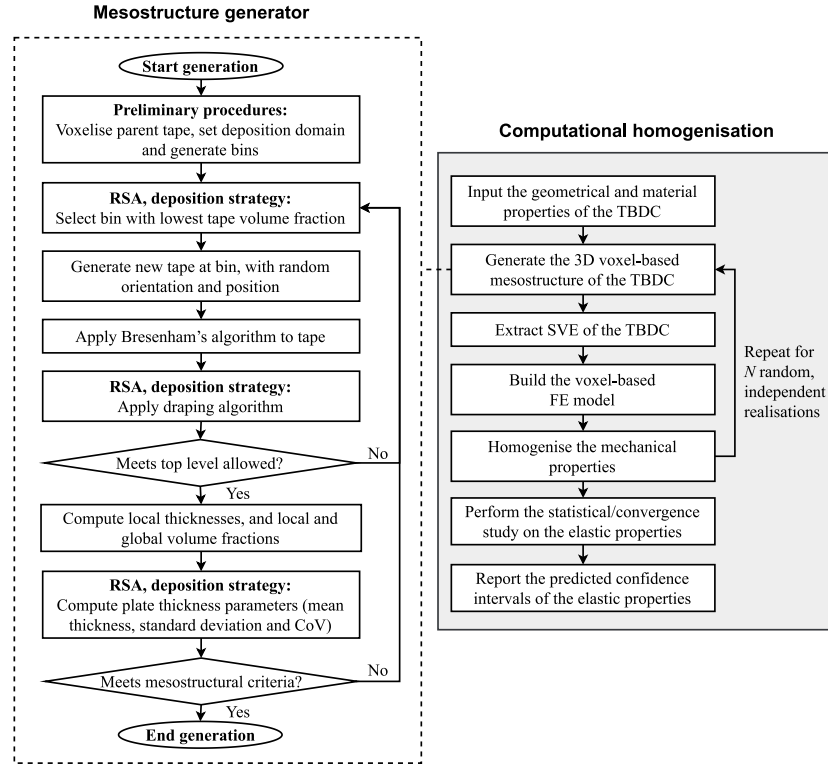
Mesostructure generator

Fig. 2. Proposed 3D mesostructure generator for TBDCs with voxelisation and random sequential adsorption procedures (left), and integration in computational homogenisation to obtain FE models of SVEs (right).

the number of voxels in the tape length $N_t^{vox,l}$ and width $N_t^{vox,w}$ are computed as

$$N_t^{vox,l} = round\left(\frac{l_t N_t^{vox,h}}{t_t R_{vox}}\right), \tag{1}$$

$$N_t^{vox,w} = round\left(\frac{w_t N_t^{vox,h}}{t_t R_{vox}}\right). \tag{2}$$

The *rounding* operator ensures an integer representation. Note that the voxel size is prescribed relative to the tape dimensions, setting the resolution of the generator in concordance with the TBDC microstructure. This implies that ultra-thin TBDCs require a higher resolution, as the number of voxels depends on t_t.

The number of voxels specify the coordinates of the parent tape in a local coordinate system (ξ, η) centred on the tape, as shown in Fig. 3(a). During the deposition, a random in-plane orientation θ and centroidal position (X_c, Y_c) are generated for each new tape, where the centroid is restricted within a selected bin (Fig. 3(b)), as explained in Section 3.3. The parent tape is translated and rotated to place it in the domain, where the resulting coordinates are specified in the global system (X, Y). Given the tape inclination, its edges are adjusted to the voxel grid using the implementation of Bresenham's algorithm by Wetzler [29,30].

3.2. Deposition domain for TBDC plate generation

By selecting the tape length as the characteristic length, the in-plane dimensions of the full deposition domain $l_D \times l_D$ (Fig. 3(b)) are chosen as a multiple M of the tape length, $l_D = M \times l_t$, such that it is larger than the virtual TBDC plate to be generated. To ensure that complete tapes can be captured in the voxel grid, the centroids are restricted within a safe domain, which is prescribed by a safe distance l_s (e.g. $l_s = l_t$) from the edges of the domain. Similarly, for the height of the domain, a top level limit Z_{limit} is allowed, and the value depends on desired mean plate thickness and the plate thickness control strategy described later.

3.3. Modified 3D-RSA and deposition strategies

A modified 3D-RSA algorithm [22,23] generates the TBDC plate by sequentially adding tapes to the domain following three strategies (Fig. 2): bin-guided allocation, tape draping, and plate thickness control.

The first strategy is the bin-guided allocation, similar to the one presented by Shah et al. [21], where the safe domain is subdivided into bins (Fig. 3(b)) to guarantee a more uniform deposition, avoiding pile-ups of tapes. However, the strategy proposed here has three key differences compared to the one in [21]:

1. Instead of selecting bins sequentially, the bin with the lowest current tape volume fraction in the iteration is chosen. The tape volume fraction in a bin is computed as the number of tape voxels in the bin over the total number of voxels in the bin as

$$V_T^{bin} = \frac{N_{vox,tapes}}{N_{vox,bin}}. \tag{3}$$

2. The thickness of the TBDC plate is not subdivided into layers with a predefined height and tape spacing as in [21]. This allows the tapes to come into contact to achieve higher tape volume fractions.

3. The number of tapes per bin is not limited to a fixed number of iterations as in [21].

The partition into bins should be coarse rather than fine. Otherwise, piles of tapes may be generated around small empty bins near the edges of the tapes. The allocation is pseudo-random since the tape centroids are chosen randomly within the subdomain of the selected bin, i.e. $X_c \in X_{bin}$ and $Y_c \in Y_{bin}$. In-plane tape orientations are generated by randomly sampling a uniform distribution over the interval $\theta \in [0°, 179°]$. Note that other orientation distributions could be used to study plates with preferred orientations (Section 5.4).
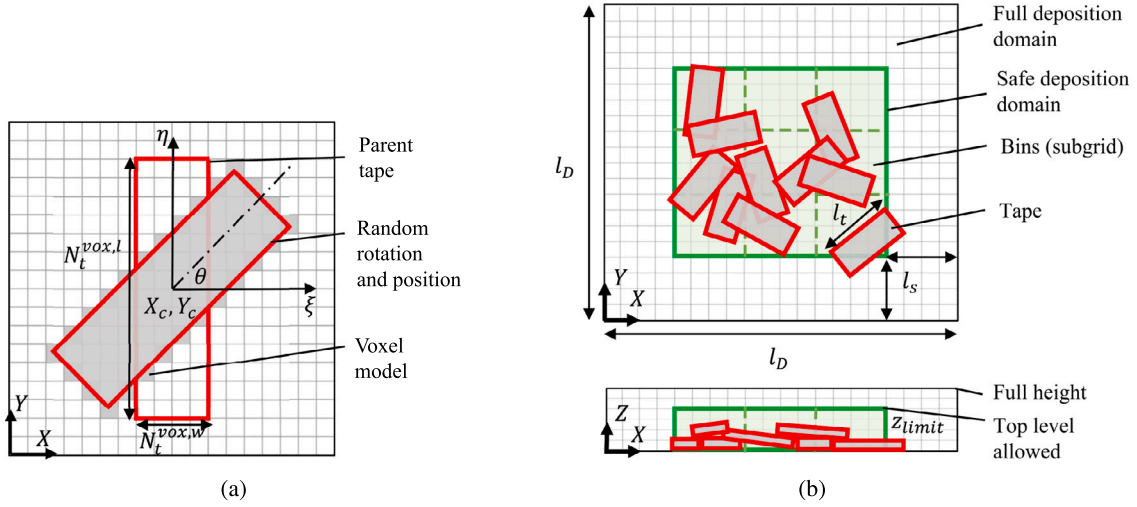
Fig. 3. Voxel-based model of tapes and TBDC domain. (a) In-plane voxelisation and Bresenham's algorithm after rotation, (b) Deposition domain with a safe space (green area) and a top level limit to capture full tapes. (For interpretation of the references to colour in this figure legend, the reader is referred to the web version of this article.)
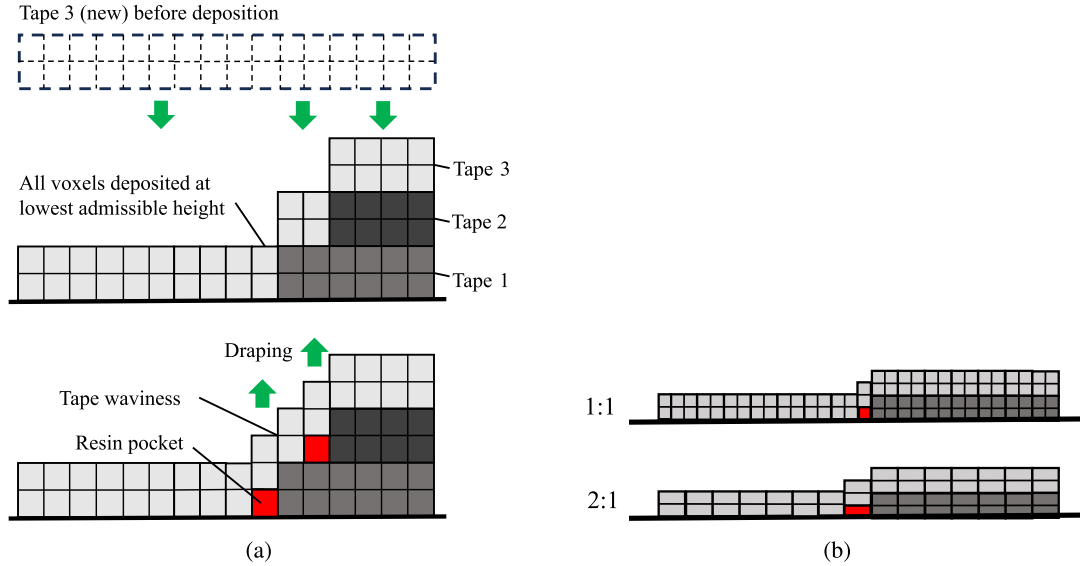

Fig. 4. Deposition algorithm with tape draping. (a) Waviness and resin pockets introduced by repositioning voxels at different heights, (b) Draping for ultra-thin tapes with R_{drap} of 1:1 and 2:1.

The second strategy is the tape draping, inspired from [22], which introduces two key mesostructural features, namely the tape waviness and the resin pockets (Fig. 4), without causing interpenetration. Ryatt et al. [22] set the tape position to a given height and use an advancement routine to deposit them. Here, to avoid excessive iterations in the advancement routine, it is instead proposed to deposit the voxels at their lowest admissible positions as illustrated in Fig. 4(a). Then, the tape discontinuities are eliminated by moving the voxels upward so that the height difference between two adjacent voxels of the same tape is not greater than a draping ratio R_{drap}, pre-defined as the number of voxels in the length or width per voxel in height used for draping. Since the draping ratio affects both the tape waviness and the resin pockets, its value should be chosen to best approximate the tape inclination (caused by draping) and the volume fraction of resin pockets observed in experimental images. Draping affects thick tapes differently from ultra-thin tapes, in terms of waviness and resin pockets, as shown in Fig. 4(b) for draping ratios 1:1 and 2:1.

The final deposition strategy involves the control of the thickness variations of the TBDC plate. This is a modified approach based on the strategies in [15]. For this, the local plate thickness $(t_p)_{ij}$ at each in-plane voxel position ij of the domain is defined as the highest voxel position occupied by the tapes, $(t_p)_{ij} = (Z_{max})_{ij}$. Then, the mean value of the plate thickness $t_{p,mean}$, its standard deviation, and its Coefficient of Variation (CoV) are calculated during the iterations of the random deposition. The random thickness variations observed in real TBDC plates are then replicated by using these measures to restrict the top-level allowed Z_{limit} (Figs. 3(b) and 5) to one standard deviation above the mean thickness $t_{p,mean} + t_{p,mean} \times CoV$. If a deposited tape exceeds the height limit, then it is discarded and a new tape is randomly generated in a new position. Finally, the generation stops when the target values for the mean plate thickness, CoV of the thickness, and global fibre volume fraction of the TBDC are within specified tolerances.

3.4. Computation of geometrical features of the TBDC plate

The local and global fibre volume fractions of the TBDC plate are computed respectively as

$$(V_f^p)_{ij} = \frac{1}{N_k} \sum_{k=1}^{N_k} D_{ijk}^{binary} V_f^t, \tag{4}$$

Table 3
UD tape and matrix elements for the FE model of TBDCs.

Element type	Material model	Properties
Tape element (C3D8)	Transverse isotropic elastic	E_1 $E_2 = E_3$ $G_{12} = G_{13}$ G_{23} $v_{12} = v_{13}$ v_{23}
Matrix element (C3D8I)	Isotropic elastic	E_m, v_m

$$V_f^p = \frac{1}{N_i N_j} \sum_{i=1}^{N_i} \sum_{j=1}^{N_j} (V_f^p)_{ij}, \tag{5}$$

where N_i, N_j and N_k are the number of voxels in the 3D array of the plate; V_f^t is the fibre volume fraction in the tapes; and D^{binary} is a 3D array of the domain D storing an entry equal to 1 for the voxels occupied by tapes and 0 for the matrix. The local and global volume fraction of tapes, $(V_T^p)_{ij}$ and V_T^p, are computed in an analogous way, removing the factor V_f^t from the previous equations.

The local and global mean in-plane tape angles are also of interest, $(\theta_p)_{ij}$ and θ_p, and are calculated by taking the mean of the in-plane tape angles through the thickness and for the whole domain, respectively. The mean angles allow a quantification of the randomness of the tape orientations in TBDCs, as for a completely random distribution of the in-plane tape angles the mean value is 45°. Out-of-plane angles are discussed in Section 5.2.

4. Application to mechanical simulations

This section presents the application of the 3D mesostructural generator in the prediction of homogenised elastic properties of TBDCs. Other potential applications are discussed in Section 5.4.

4.1. Finite element model of TBDCs

The output data of the generator contains the tape locations, the tape orientations, and the resin pockets, and its used to build a 3D FE model in ABAQUS [31] via an automated input file writer. The mesh matches the discretisation inherently created by the voxelisation procedure. Consequently, the cuboid voxels define 8-node continuum elements, both for the matrix (C3D8I) and the tapes (C3D8). In this case, 8-node trilinear elements are chosen to reduce the computational cost. This is especially important in the case of ultra-thin tapes that demand a higher resolution. However, the methodology is general and allows the use of higher-order elements. Since the matrix is a soft phase, C3D8I elements are used. Compared to the standard C3D8 elements, C3D8I are first-order elements including incompatible deformation modes to eliminate the parasitic shear stresses leading to over-stiffness (shear-locking) [31].

In terms of material models, an isotropic linear elastic model is used for the matrix with the elastic modulus E_m and Poisson's ratio v_m, and a transversal isotropic linear elastic model for the UD tapes, with the elastic moduli (E_1, E_2, E_3), shear moduli (G_{12}, G_{13}, G_{23}), and Poisson's ratios (v_{12}, v_{13}, v_{23}) as given in Table 3. These assumptions are consistent with those used in the literature (e.g. see [23]). The properties of the UD tapes can be obtained either from material data-sheets or computed from classic micromechanics.

4.2. Homogenisation of mechanical properties

In this study, the main objective is to obtain the homogenised elastic properties of TBDCs, e.g. E_x, E_y, and G_{xy}. Given the in-plane quasi-isotropic response of TBDCs [2], then $E_x = E_y = E$ and G.
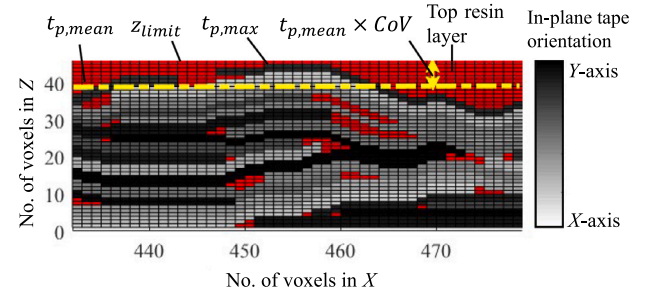

Fig. 5. Plate thickness control. Matrix is shown in red and tapes in grey-scale according to their orientation. (For interpretation of the references to colour in this figure legend, the reader is referred to the web version of this article.)

Several homogenisation techniques have been studied in the literature for multi-phase composites, and their applicability depends on the type of heterogeneities in the material system. In particular, TBDCs are far from behaving like a two-phase material as each reinforcing tape has a different 3D local geometry and orientation affected by draping/waviness, and variations in cured tape properties can also be introduced by compaction effects and resin bleeding (Section 2.2). Moreover, the volume fractions of fibre and tapes are both considerably high. In such cases, with randomly oriented/shaped inclusions with anisotropy, direct mean-field Eshelby-based homogenisation has been shown to produce non-symmetric stiffness tensors, leading to unphysical predictions [32]. A two-step homogenisation, where the SVE is decomposed first into grains, is difficult to apply as it is challenging to approximate the tape shapes as Eshelby ellipsoids. Even combining a FE computation of strain concentration tensors with mean field schemes may still produce non-symmetric stiffness tensors [33].

To overcome the above difficulties in TBDCs, a fully FE-based approach to SVE homogenisation is chosen for this study. With the EasyPBC plugin for ABAQUS [34], standard 3D computational homogenisation with periodic boundary conditions is applied to predict the elastic properties. Previous studies have shown that periodic boundary conditions produce better approximations of the effective elastic properties of complex composite microstructures compared to other boundary conditions [35], even for non-periodic microstructures. A key factor in computational homogenisation is the size and sampling of SVEs. Since the microstructure is random, a statistical study is required, which is described next.

4.3. Statistical analysis and convergence study

The subsequent simulations require a statistical analysis of different properties, either geometrical or mechanical, in terms of mean values (μ) and standard deviations (S) computed as (for statistical samples a_i)

$$\mu = \frac{1}{N_{sim}} \sum_{i=1}^{N_{sim}} a_i, \tag{6}$$

$$S = \sqrt{\frac{1}{N_{sim} - 1} \sum_{i=1}^{N_{sim}} |a_i - \mu|^2}. \tag{7}$$

To study convergence, the Cumulative Average (CA) and cumulative standard deviation up to n realisations are used,

$$\mu_n^{CA} = \frac{1}{n} \sum_{i=1}^{n} a_i, \tag{8}$$

$$S_n^{CA} = \sqrt{\frac{1}{n-1} \sum_{i=1}^{n} |a_i - \mu_n^{CA}|^2}. \tag{9}$$
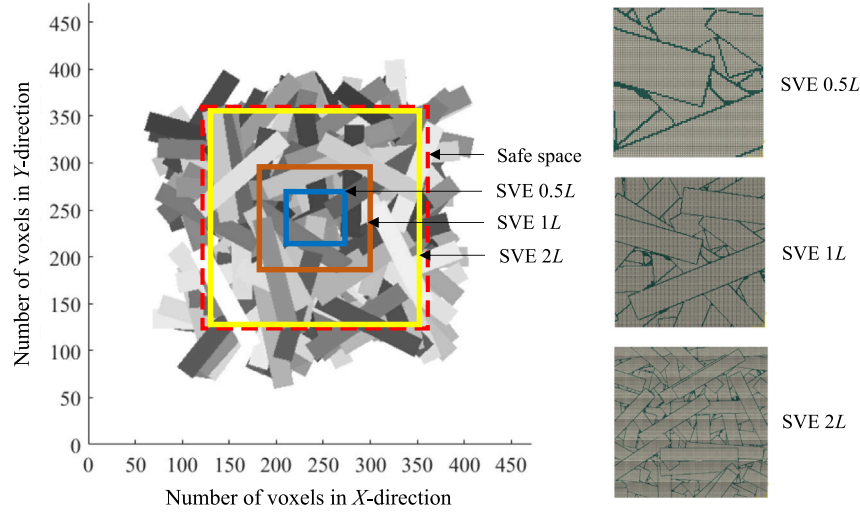
Fig. 6. Example of virtual realisations of full 3D plates of the thick TBDC and extraction of SVEs.

From these, the absolute and relative errors of the statistics are [36],

$$(\varepsilon_{abs})_n^{CA} = \frac{z_{CI} S_n^{CA}}{\sqrt{n}}, \tag{10}$$

$$(\varepsilon_{rel})_n^{CA} = \frac{z_{CI} S_n^{CA}}{\mu_n^{CA} \sqrt{n}}, \tag{11}$$

where z_{CI} depends on the desired Confidence Interval (CI). In this study, a CI of 95% is used, thus $z_{CI} = 1.96$. The estimation of the properties using CI is provided in the form $\mu_n^{CA} \pm (\varepsilon_{abs})_n^{C}$. As convergence criterion, a 5% tolerance or less is set on the error, which is generally acceptable in the literature [36].

4.4. Determination of the SVE size for TBDCs

The SVEs should capture a sufficient number of microstructural heterogeneities to model its macrostructural properties, which assumes a scale separation $L_{micro} \ll L_{meso} \ll L_{macro}$ [37], where L_{micro}, L_{meso}, and L_{macro} are the characteristic lengths at the micro-, meso- (SVE), and macrostructural levels, respectively. In fibre-reinforced composites, L_{micro} is generally the fibre diameter d_f or length l_f, where $L_{meso}/d_f > 18$ and $L_{meso}/l_f > 1.5$ are typical [37,38]. However, few studies have investigated the scales in TBDCs [20]. The current study identifies the following considerations when determining an appropriate SVE size for TBDCs: (1) the in-plane sizing of the SVE required to capture enough tape orientations; (2) strategies to obtain a uniform SVE thickness from the virtual plate; (3) the generation of statistically independent realisations in accordance with the random nature found in experiments; (4) an assessment of computational cost in terms of the number of realisations and convergence of the elastic properties. These aspects are discussed next.

In TBDCs, by choosing the tape length (major mesostructural feature) as the characteristic length $L = l_t$ for the SVE sizing, it is ensured that the microstructure is captured. Then, the SVE size is specified as $mL \times mL \times t$, where $m = L_{meso}/L$ and t is the SVE thickness [20]. In principle, the ideal size of the SVE is defined as the volume required to estimate the effective elastic properties within a given error using a single realisation. In practice, different SVE sizes are evaluated with respect to the tape size, and the number of realisations for the convergence of the elastic properties, as well as their standard deviation, confidence intervals, and errors are studied. The statistical approach is to choose a smaller SVE and average n realisations until the desired relative error is achieved [39]. Here, the following sizes are studied: $0.5L$, $1L$, and $2L$.

As shown in Table 2, the tape dimensions for the three cases are similar, except for the thickness. Thus, the number of tapes through the plate thickness is higher for the ultra-thin (approx. 50) than for the thick TBDC (approx. 7), the later containing a lower number of heterogeneities ("worst" scenario). Hence, the thick TBDC is chosen as a prototype to study the SVE size, thereby also reducing the computational cost.

Some considerations are needed to extract the SVEs from the generated TBDC plates. To ensure independent realisations and avoid edge effects, a new deposition of the plate is generated for each realisation and the SVE is extracted from the central region of the safe domain (Figs. 3(b) and 6). For this purpose, the domain is sized using $l_D = 4 \times l_t$ and $l_s = l_t$, where l_t is the tape length. In turn, the safe domain is divided into 4 bins in total (2×2 subgrid) for the bin-guided allocation strategy. For the prototype case of the thick TBDC, two voxels per tape thickness $N_t^{vox,h} = 2$ and a voxel aspect ratio $R_{vox} = R_{drap} = 1.38$ are set for the SVE sizes $0.5L$ and $1L$. For the SVE $2L$, $N_t^{vox,h} = 1$ and $R_{vox} = R_{drap} = 2.45$ are used to reduce the computational cost. These parameters result in a mean resin pocket volume fraction between 4.7 and 5.5%, which is consistent with values reported in the literature (Section 2.2).

Another consideration is related to the SVE thickness because the plate has a varying thickness, and the virtual model introduces a top resin layer to populate such a variation in the domain (Fig. 5). Since the top resin layer adds an artificial compliance to the model, it is cut by restricting the height of the domain to produce a uniform SVE thickness, while meeting the mean plate thickness, and the global tape and fibre volume fractions. This highlights the advantage of implementing the plate thickness control strategy (Section 3.3), whereby controlling the thickness CoV the effect of the top resin layer can be reduced.

Finally, to assess the randomness in the plates, a statistical study of the mean tape angle is used. The generated mean in-plane tape angle is compared to $45°$, which represents complete randomness in the in-plane orientations when all possible values $\theta \in [0°, 179°]$ are mapped into the first quadrant, due to symmetry.

4.5. Prediction of elastic properties and comparisons

For each case study, an SVE size is chosen and the corresponding number of FE simulations for different realisations are run until convergence of the mechanical properties of the TBDC (i.e. E_x, E_y, and G_{xy}) is achieved based on a 5% relative error, or lower, in the 95% confidence intervals. The model is assessed by comparing the values with experimental results from the literature (Table 1).

Table 4
Convergence study for the thick TBDC. Predicted properties and no. of realisations for convergence (N_{conv}).

SVE	Property	N_{conv}	Mean [GPa]	Std dev. [GPa]	CI [GPa]
0.5L	θ_p	21	45.54	5.20	2.22
	E_x	46	33.15	5.61	1.62
	E_y	49	35.77	6.22	1.74
	G_{xy}	18	13.09	1.39	0.64
	v_{xy}	53	0.290	0.073	0.020
	$G_{xy} = E_x/2(1+v_{xy})$	–	12.84	–	–
1L	θ_p	9	44.21	3.32	2.17
	E_x	14	34.65	3.28	1.72
	E_y	16	33.66	3.47	1.7
	G_{xy}	2	13.04	0.05	0.07
	v_{xy}	16	0.296	0.033	0.016
	$G_{xy} = E_x/2(1+v_{xy})$	–	13.36	–	–
2L	θ_p	7	45.03	2.94	2.18
	E_x	14	35.80	3.31	1.73
	E_y	15	36.34	3.61	1.89
	G_{xy}	2	13.76	0.02	0.03
	v_{xy}	15	0.283	0.029	0.015
	$G_{xy} = E_x/2(1+v_{xy})$	–	13.95	–	–

5. Results and discussion

5.1. SVE sizing for TBDCs

Fig. 6 illustrates the capability of the method to generate virtual realisations of full 3D TBDC plates, and how different SVE sizes can be extracted and exported to FE models in ABAQUS to obtain the homogenised elastic properties. The thick TBDC has been used as the prototype case.

5.1.1. Convergence of geometrical and mechanical properties

First, the geometrical aspects are discussed. The randomness is assessed by comparing θ_p with 45°, the theoretical value indicating complete randomness. To analyse the different SVE sizes, the CA of θ_p was evaluated until convergence (Fig. 7). As expected, for a small SVE size such as 0.5L, there are fewer tapes and the SVE is less probable to contain all possible orientations (Fig. 6). This may result in a dominant orientation rather than being completely random. The consequence is evidenced in Fig. 7(a) with variations in the CA of θ_p, requiring a larger number of realisations to converge to 45°. The same behaviour is expected in SVEs smaller than 0.5L. When the SVE size increases, e.g. to 1L, more tapes and more orientations are taken into account (compare 0.5L and 1L in Fig. 6), thus the variations dissipate faster. This is even more prevalent for the size 2L, suggesting that a size of 2L or larger captures the randomness of TBDCs with the considered length to thickness ratio.

Further insight can be obtained from the histograms of θ_p for several realisations (Fig. 8). In small SVEs such as 0.5L, dominant directions occur rather than being completely random, wherein variations in θ_p of almost ± 20° with respect to 45° are observed. On the other hand, in SVE sizes of 2L, the distribution is more narrow and the variations are around ± 5°, therefore neither the Y- or X-directions are considered to be dominant. The histogram for the SVE size of 1L is very similar to that of 2L.

Next, the mechanical aspects are discussed. Specifically, the effect of the SVE size on the homogenised elastic properties is of interest. The results are shown in Table 4 and Fig. 7, where the mean value, standard deviation, CI, and the number of realisations until convergence (N_{conv}) with errors <5% are given.

An important result is that the predicted mean value of E_x and E_y converged to very close values for each SVE size, which is expected as θ_p converges to 45°, indicating an in-plane isotropic behaviour. This is consistent with the findings in the literature [2]. For comparison, the value obtained with the isotropic relation $G_{xy} = E_x/2(1+v_{xy})$ is

included in Table 4, where the difference with respect to the numerical value of G_{xy} becomes smaller for larger SVEs.

Since the CI is similar at convergence, the main difference is in the required N_{conv} and the standard deviations, where smaller SVEs need larger N_{conv} and result in larger standard deviations. By comparing the necessary number of realisations for a converged θ_p to those necessary for obtaining converged elastic parameters, it is clear that N_{conv} of θ_p is generally lower. Furthermore, the standard deviations of E_x and E_y are similar to those of θ_p for all SVE sizes, while the standard deviations of G_{xy} are always smaller, suggesting that the Young's moduli are more sensitive to the tape orientations. Fig. 7 additionally shows the CA of the mean value $(E_x + E_y)/2$, which clearly converges much faster and requires fewer realisations, indicating that it can be used as a reliable statistical estimator for the Young's moduli.

It is also possible to link the trends observed in Fig. 7. For instance, when θ_p is less than 45°, the dominant orientation is in the X-direction and E_x is greater than E_y. Thus, E_x and E_y converge with opposite trends. Such a strong dependence is not evident with the shear modulus G_{xy}.

Although the CI (error) of the properties is essentially equal, the implications for the simulations should be highlighted. It is possible to achieve convergence with small SVEs such as 0.5L, or smaller, by virtue of the averaging of a larger number of realisations. However, single small SVEs are not statistically representative for TBDCs in the sense that they are not random and contain dominant orientations.

The previous results show the differences between geometrical and mechanical convergence. It is apparent that a statistically representative geometry is a key factor. However, the findings show that the relation between θ_p and the various elastic moduli is different (Table 4). The Young's modulus shows a strong dependence on θ_p in terms of the trends of the values, their standard deviations and the number of realisations required for convergence, indicating that it can be considered as a necessary condition for its convergence. On the other hand, the shear modulus does not show such sensitivity, which is observed in the need of fewer realisations to converge. These differences can be exploited in the simulations to choose more efficiently the number of realisations required, depending on the elastic properties of interest to be predicted.

5.1.2. Mesh sensitivity and computational cost

The effect of coarsening voxel-based meshes on the elastic properties of TBDCs have been investigated in the literature. Ryatt and Ramulu [23] found that in-plane coarsening by a factor of 2 to 4, and through the thickness by a factor of 3, produce effective properties comparable to detailed models as long as the volume fraction of resin pockets is approximately the same. In the present study this has been verified by comparing the meshes of SVE sizes of 1L and 2L, where a coarsening through the SVE thickness by a factor of 2 produced a variation of around 3%–4%, depending on the property and the setting of R_{vox} and R_{drap}.

Finally, some remarks are made regarding the simulation times. The generation times of the geometry do not vary considerably with the SVE size, as a larger safe domain is always generated to extract the SVEs. The computational times are mainly increased by the FE simulations. From Fig. 9, the major advantage of using small SVEs is to reduce the simulation times, while the advantage of using large SVEs is to reduce the number of realisations and the standard deviation of the results (Table 4). The accuracy of the predicted CI is the same, illustrating the benefit of this statistical study. This allows for flexibility and trade-off in the modelling. Thus, working with smaller SVEs (e.g. 0.5L or smaller) tends to be more efficient, while still fulfilling the convergence criteria (Section 4.3). As mentioned above, the choice of the SVE size also involves assessing whether a statistically representative geometry is required.
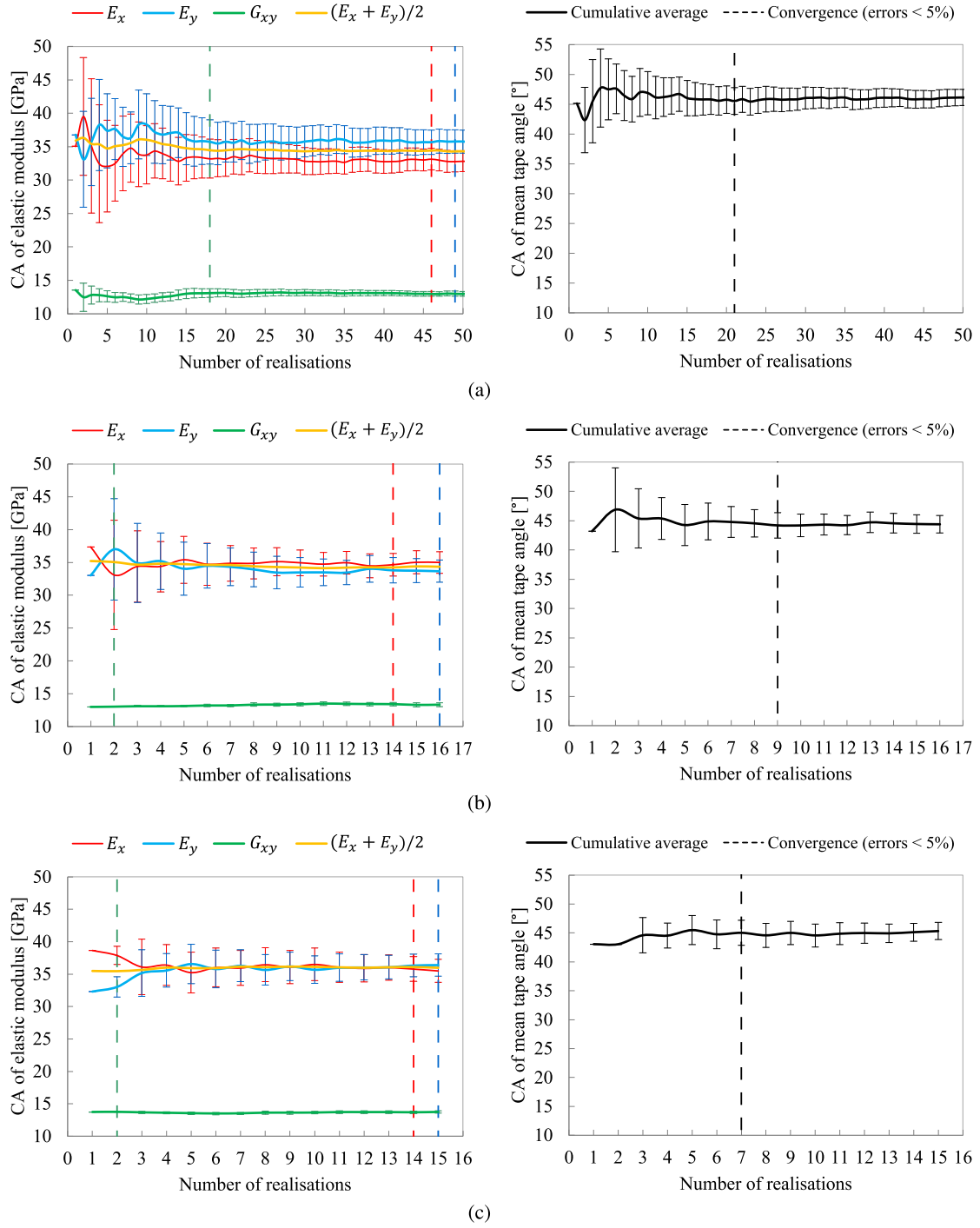
Fig. 7. Convergence study for different SVE sizes of the thick TBDC. The Cumulative Average (CA), Confidence Intervals (CI), and number of realisations for convergence (N_{conv}, dashed lines) are given for the predicted properties and the mean in-plane tape angle of each SVE. (a) SVE 0.5L, (b) SVE 1L, (c) SVE 2L.

5.2. Out-of-plane angle distributions

To analyse the out-of-plane tape angles caused by draping (waviness), a procedure similar to the one proposed by Alves and Pimenta is followed [11], as presented in Fig. 10(a). The centreline of each tape is discretised by using a pre-defined spacing resolution S_c (number of voxels), then the local out-of-plane angle φ of each path segment is calculated, and finally these angles are averaged to obtain the mean out-of-plane angle of each tape φ_t. By adjusting the spacing resolution S_c, the extracted centreline can be smoothened.

Fig. 10(b) shows the predicted distributions of the mean out-of-plane tape angles for the three TBDCs. The angles φ_t are between −14° and 14° for the thick TBDC, between −6° and 6° for the thin TBDC, and between −4° and 4° for the ultra-thin TBDC. As expected, the mesostructures tend to be more flattened and less wavy when the tapes are thinner [3,6]. In the ultra-thin TBDC, at least 97% of the tapes are predominantly flat (−2° ≤ φ_t ≤ 2°) and show less variability, in contrast to the 77% and 47% in the thin and thick TBDCs, respectively. Although the available experimental data is limited, the values for thicker TBDCs are consistent with those reported in the literature [11]. This demonstrates the capability of the proposed 3D mesostructural
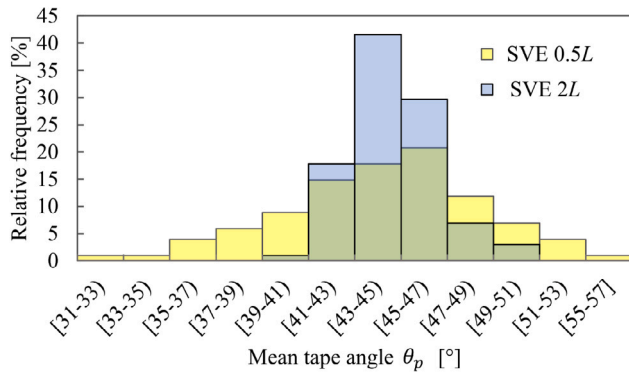
Fig. 8. Histogram of the mean in-plane tape angle distributions for 100 SVE realisations of the thick TBDC.
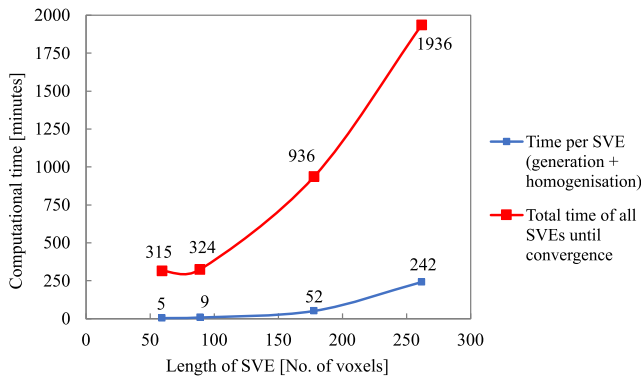

Fig. 9. Computational times for the SVEs of the thick TBDC with $R_{vox} = R_{drap} = 2$. PC specifications: 12th Gen Intel(R) Core (TM) i7-1265U, 10 cores, 1.8 GHz, 32 GB RAM.

Table 5
Comparison between predicted and experimental values (see Table 1).

TBDC	Method	V_f^p	E [GPa]	G [GPa]
Thick	Numerical, FE	53.54 ± 0.72	34.46 ± 1.68[a]	13.09 ± 0.64
	Experimental	53.50 ± 5.39	39.66 ± 5.06	–
	Analytical, EL	53.50	47.94	18.42
Thin	Numerical, FE	55.25 ± 0.23	40.21 ± 1.43[a]	15.61 ± 0.28
	Experimental	57.85 ± 3.84	43.41 ± 4.14	–
	Analytical, EL	57.85	51.28	19.66
Ultra-thin	Numerical, FE	62.02 ± 0.18	65.23 ± 3.06[a]	24.09 ± 0.65
	Experimental	62.69 ± 5.69	69.9 ± 3.2	25.64[b]
	Analytical, EL	62.69	70.73	26.54

[a] From mean value $E = (E_x + E_y)/2$.

[b] From $G = E/2(1 + v)$ and values in Table 1.

generator to reproduce the out-of-plane spatial variability found in different types of TBDCs.

5.3. Homogenised elastic properties and comparison with experimental data

Based on the considerations discussed in the previous sections, this section presents the results obtained by applying them to the thick, thin, and ultra-thin TBDC case studies described in Section 2.

An SVE size of $0.5L$ was used for the thick and thin cases, and $0.25L$ for the ultra-thin case to reduce the computational cost while fulfilling the convergence criteria (Sections 4.3 and 4.5) as discussed before. To generate the mesostructures, the deposition domains were sized based on $l_D = 4 \times l_t$. The safe distance used was $l_s = l_t$, and the safe domains were divided into 4 bins. For the thick and thin cases, the resolution is lower because the thicknesses of the tapes are larger, requiring less voxels to capture their geometry compared to the ultra-thin case. The parameters for the thick TBDC were provided in Section 4.4. For the thin case, $N_t^{vox,h} = 1$ and $R_{vox} = R_{drap} = 1.7$ were used, in contrast to $R_{vox} = R_{drap} = 7.7$ set for the ultra-thin TBDC. This exploits the draping principle shown in Fig. 4, where it is apparent that ultra-thin tapes can accommodate larger ratios to achieve the corresponding resolution because the voxelisation is done relative to their thickness. This is consistent with the fact that the resin pocket content is higher in thicker TBDCs than in ultra-thin TBDCs. For instance, with these parameters, a mean resin pocket volume fraction of 2.64% was obtained for the thin TBDC, while for the ultra-thin TBDC was 1%, both lower than that of the thick TBDC. These values are consistent with those obtained from the microscopic image analysis and the values reported in the literature (Section 2.2).

The mean fibre volume fractions of the virtual TBDC plates are reported in Table 5. Depending on the settings of the resin content, it

is possible that the model underpredicts the values of the global fibre volume fractions, since it neglects aspects related to compaction and resin bleeding.

Table 5 and Fig. 11 summarise the predictions of E (mean of E_x and E_y) and G, together with results from analytical ELs similar to the one proposed in [2]. The ELs have a quasi-isotropic lay-up $[45/-45/90/0]_s$. It is observed that the predictions with the analytical ELs tend to be higher, which can be explained by the fact that the draping is neglected and therefore the lack of crimp allows to obtain higher stiffness compared to both experimental and numerical values. Despite being fast to implement, the main disadvantage of ELs is the tendency to overestimate the properties and the difficulty in assessing variability. In comparison, and considering the uncertainty of input data, the numerical values of the stiffnesses are considered to be in good agreement with the experimental data, with an error of 13.1% for the thick case, 7.4% for the thin case, and 6.7% for the ultra-thin case. The error on the shear modulus of the ultra-thin TBDC is 6%. The predictions of E_x and E_y were close for all cases, again confirming the in-plane isotropy.

Several sources of error can be identified. For instance, tape compaction and other processing effects during consolidation are neglected, which affect the cured properties. Also, tape properties are commonly scaled from the limited experimental data available for different fibre volume fractions. In turn, the measurements of the fibre volume fraction of plates/tapes have exhibited a high scatter (Section 2.2).

5.4. Future implications and potential impact

In general, full 3D TBDC plates obtained with the mesostructural generator can be readily post-processed to obtain input geometries and FE models required for different types of analysis and applications.

The presented framework has been shown to be effective for predicting the elastic properties of thick, thin, and ultra-thin TBDCs. It also shows the limitations of analytical methods such as ELs. By explicitly capturing the tape geometry, the generator allows to perform parametric studies on shape aspect ratios and tape properties with the aim of obtaining desired plate properties. This aids in reducing time and cost in the optimisation of TBDCs, a process that is currently done predominantly on an experimental basis. Moreover, it allows for the quantification and scale-up of variability in relation to mesostructural features, which is important for determining design allowables. The incorporation of a tape angle distribution also enables the study of plates with preferred orientations. Thereby, the framework could be used to determine tape orientation distributions that yield non-isotropic elastic macroscale properties tailored to specific applications and requirements.

The voxelised model proposed in this study can potentially be combined with post-processing strategies to alleviate spurious stress concentrations resulting from the voxelised geometry. Thereby, there is a future potential to also study damage and strength of TBDCs,
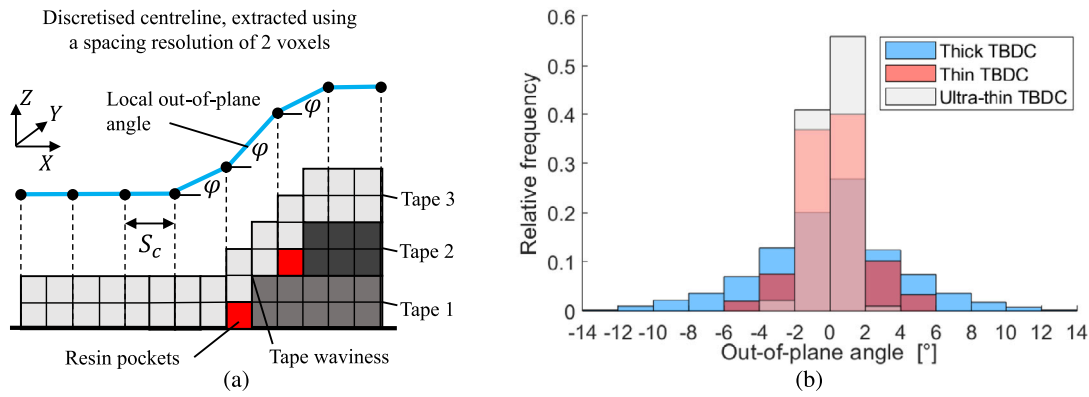
Fig. 10. Out-of-plane angles in TBDCs. (a) Calculation from discretised centreline, (b) Predicted distributions.
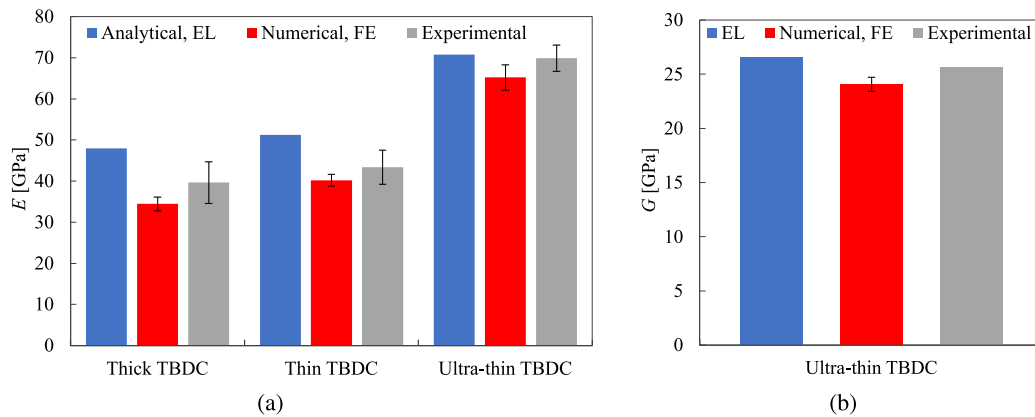

Fig. 11. Comparison between the predicted and the experimental values (Table 5). (a) Young's modulus of the three TBDCs, (b) Shear modulus of the ultra-thin TBDC. Experimental value estimated using $G = E/2(1 + v)$.

while carefully accounting for their 3D mesostructure. For instance, local stress averaging techniques with customised damage tracking algorithms have proven to give stress distributions similar to those obtained by conformal meshes of tow-based composites [40]. More-over, such a technique captures the stress distributions at the tow interfaces, allowing debonding cases to be studied with acceptable accuracy. Alternatively, smoothed models can be obtained by post-processing the voxelised geometry using a level-set representation and applying Gaussian filtering [41]. In turn, a representation based on level-sets would allow to explore new advanced meshing techniques to incorporate cohesive elements between smoothed tow interfaces and study damage, as proposed e.g. by Li et al. [42].

6. Conclusions

Novel ultra-thin TBDCs have recently been under development to increase the stiffness and strength of thick and thin TBDCs. However, limited research has been conducted on numerical models that cap-ture their complex 3D microstructure, which affects their mechanical response. This paper presents a numerical framework to generate 3D voxel-based mesostructures using a modified 3D-RSA to predict the homogenised elastic properties of thick, thin, and ultra-thin TBDC case studies via FE models.

The proposed 3D-RSA method extends strategies from the litera-ture [15,21,22] by combining: (i) a bin-guided deposition to obtain a uniform spatial distribution; (ii) a draping method to produce tape waviness and resin pockets; and (iii) a control strategy to obtain

random plate thickness variations. The capabilities of the method are demonstrated by generating different TBDCs with realistic fibre volume fractions, between 53 and 63%, and mean resin pocket volume fractions between 1 and 6%, in agreement with experiments. The out-of-plane angle distributions also prove the ability to reproduce the spatial variation of TBDCs.

A statistical study is carried out to assess the effect of different SVE sizes on the homogenised elastic properties (E_x, E_y, and G_{xy}). In small SVEs such as $0.5L$, it is found that dominant mean tape orientations may occur instead of being completely random, requiring a larger number of realisations to achieve convergence of the elastic properties. When the SVE size is increased, e.g to $2L$, the number of realisations needed is reduced by at least 4 times. A trade-off is necessary to reduce the computational cost, thus it is more efficient to work with smaller sizes. In all cases the in-plane quasi-isotropic response is verified.

Finally, the numerical framework is used to predict the homog-enised elastic properties of the thick, thin, and ultra-thin cases, showing good agreement with the experimental values with errors between 6 and 13%, where errors were lower for thinner TBDCs. In all cases, the numerical results are conservative and under-predicted the properties. This is attributed to the fact that the fibre volume fractions obtained with the model tend to be slightly lower than the real ones, since the model does not take into account aspects such as compaction and resin bleeding. These introduce greater uncertainty in the cured tape properties, for which there is also limited experimental data and the properties are commonly scaled in the literature. On the other hand, the analytical EL models over-predicted the properties, as draping and

resin pockets are neglected, giving larger errors for thicker TBDCs (up to 20%).

The proposed framework provides a tool to generate 3D FE models of TBDCs with realistic fibre volume fractions and mesostructural features, which serves for future work in materials optimisation, and damage studies that require a more detailed description than is provided by EL models or 2D models.

CRediT authorship contribution statement

Luis Gulfo: Writing – original draft, Validation, Software, Methodology, Investigation, Conceptualization, Formal analysis, Visualization. **Olle Haglund Nilsson:** Software, Methodology, Investigation. **Jacob Sjöberg:** Software, Methodology, Investigation. **Ioannis Katsivalis:** Writing – review & editing, Supervision, Formal analysis, Investigation. **Leif E. Asp:** Writing – review & editing, Supervision, Funding acquisition. **Martin Fagerström:** Writing – review & editing, Supervision, Resources, Project administration, Methodology, Conceptualization.

Declaration of competing interest

The authors declare that they have no known competing financial interests or personal relationships that could have appeared to influence the work reported in this paper.

Data availability

Data will be made available on request.

Acknowledgements

References

[1] DoD USA. MIL-HDBK-17-1F composite materials handbook. 2002.

[2] Katsivalis I, Persson M, Johansen M, Moreau F, Kullgren E, Norrby M, Zenkert D, Pimenta S, Asp L. Strength analysis and failure prediction of thin tow-based discontinuous composites. Compos Sci Technol 2024;245:110342.

[3] Alves M, Carlstedt D, Ohlsson F, Asp L, Pimenta S. Ultra-strong and stiff randomly-oriented discontinuous composites: Closing the gap to quasi-isotropic continuous-fibre laminates. Composites A 2020;132:105826.

[4] Wulfsberg J, Herrmann A, Ziegmann G, Lonsdorfer G, Stöß N, Fette M. Combination of carbon fibre sheet moulding compound and prepreg compression moulding in aerospace industry. Proc Eng 2014;81:1601–7.

[5] Al-Furjan M, Shan L, Shen X, Zarei M, Hajmohammad M, Kolahchi R. A review on fabrication techniques and tensile properties of glass, carbon, and Kevlar fiber reinforced polymer composites. J Mater Res Technol 2022;19:2930–59.

[6] Li Y, Pimenta S, Singgih J, Nothdurfter S, Schuffenhauer K. Experimental investigation of randomly-oriented tow-based discontinuous composites and their equivalent laminates. Composites A 2017;102:64–75.

[7] Görthofer J, Schneider M, Ospald F, Hrymak A, Böhlke T. Computational homogenization of sheet molding compound composites based on high fidelity representative volume elements. Comput Mater Sci 2020;174:109456.

[8] Arteiro A, Furtado C, Catalanotti G, Linde P, Camanho P. Thin-ply polymer composite materials: A review. Composites A 2020;132:105777.

[9] Camanho P, Dávila C, Pinho S, Iannucci L, Robinson P. Prediction of in situ strengths and matrix cracking in composites under transverse tension and in-plane shear. Composites A 2006;37:165–76.

[10] FAA USA. DOT/FAA/TC-16/35 Certification of discontinuous fiber composite structures via stochastic modeling. 2017, https://www.tc.faa.gov/its/worldpac/techrpt/tc16-35.pdf.

[11] Alves M, Pimenta S. The influence of 3D microstructural features on the elastic behaviour of tow-based discontinuous composites. Compos Struct 2020;251:112484.

[12] Feraboli P, Cleveland T, Stickler P, Halpin J. Stochastic laminate analogy for simulating the variability in modulus of discontinuous composite materials. Composites A 2010;41:557–70.

[13] Selezneva M, Roy S, Meldrum S, Lessard L, Yousefpour A. Modelling of mechanical properties of randomly oriented strand thermoplastic composites. J Compos Mater 2016;51(6):831–45.

[14] Li Y, Pimenta S. Development and assessment of modelling strategies to predict failure in tow-based discontinuous composites. Compos Struct 2019;209:1005–21.

[15] Ko S, Yang J, Tuttle M, Salviato M. Effect of the platelet size on the fracturing behavior and size effect of discontinuous fiber composite structures. Compos Struct 2019;227:111245.

[16] Alves M, Martulli L, Kerschbaum M, Swolfs Y, Lomov S, Pimenta S. A 3D finite element stochastic framework for the failure of tow-based discontinuous composites. Compos Sci Technol 2023;232:109846.

[17] Wan Y, Takahashi J. CFRTP mechanical properties simulation by Mori-Tanaka model and equivalent laminate method. ECCM17 2016.

[18] Sommer D, Kravchenko S, Denos B, Favaloro A, Pipes R. Integrative analysis for prediction of process-induced, orientation dependent tensile properties in a stochastic prepreg platelet molded composite. Composites A 2020;130:105759.

[19] Kugler S, Kech A, Cruz C, Osswald T. Fiber orientation predictions—A review of existing models. J Compos Sci 2020;4–69.

[20] Krishna Mohan P, Anil Kumar M, Mohite P. Representative volume element generation and its size determination for discontinuous composites made from chopped prepregs. Compos Struct 2020;252:112633.

[21] Shah S, Choudhry R, Mahadzir S. A new approach for strength and stiffness prediction of discontinuous fibre reinforced composites (DFC). Composites B 2020;183:107676.

[22] Ryatt J, Ramulu M. Prediction of tensile failure of stochastic tow-based discontinuous composites via mesoscale finite element analysis. Compos Struct 2022;279:114769.

[23] Ryatt J, Ramulu M. Numerical investigation of the application of voxel based meshes for stochastic tow based discontinuous composites. Finite Elem Anal Des 2023;214:103874.

[24] Alves M, Li Y, Pimenta S. Spatial variability and characteristic length-scales of strain fields in tow-based discontinuous composites: Characterisation and modelling. Composites B 2023;262:110789.

[25] ASTM Intl. D3171 standard test methods for constituent content of composite materials. 2015.

[26] Otsu N. A threshold selection method from gray-level histograms. IEEE Trans Syst Man Cybern 1979;9:62–6.

[27] Sommer D, Kravchenko S, Byron Pipes R. A numerical study of the meso-structure variability in the compaction process of prepreg platelet molded composites. Composites A 2020;138:106010.

[28] The MathWorks, Inc. MATLAB release 2021b. 2021.

[29] Wetzler A. Bresenham optimized for MATLAB. 2010, https://se.mathworks.com/matlabcentral/fileexchange/28190-bresenham-optimized-for-matlab.

[30] Joy K. On-line computer graphics notes, bresenham's algorithm. 1999.

[31] Dassault Systèmes Simulia Corp. Abaqus/CAE User's Guide. 2022.

[32] Pierard O, Friebel C, Doghri I. Mean-field homogenization of multi-phase thermo-elastic composites: a general framework and its validation. Compos Sci Technol 2004;64:1587–603.

[33] Jain A, Jin B, Nutt S. Mean field homogenization methods for strand composites. Composites B 2017;124:31–9.

[34] Omairey S, Dunning D, Sriramula S. Development of an ABAQUS plugin tool for periodic RVE homogenisation. Eng Comput 2019;35:567–77.

[35] Tian W, Qi L, Chao X, Liang J, Fu M. Periodic boundary condition and its numerical implementation algorithm for the evaluation of effective mechanical properties of the composites with complicated micro-structures. Composites B 2019;162:1–10.

[36] Hoang T, Guerich M, Yvonnet J. Determining the size of RVE for nonlinear random composites in an incremental computational homogenization framework. J Eng Mech 2016;142(5):04016018.

[37] Savvas D, Stefanou G, Papadrakakis M. Determination of RVE size for random composites with local volume fraction variation. Comput Methods Appl Mech Engrg 2016;305:340–58.

[38] Liu H, Zeng D, Li Y, Jiang L. Development of RVE-embedded solid elements model for predicting effective elastic constants of discontinuous fiber reinforced composites. Mech Mater 2016;93:109–23.

[39] Jeulin D, Kanit T, Forest S. Representative volume element: a statistical point of view. In: Continuum Models and Discrete Systems. Kluwer Academic Publishers; 2004, p. 21–7,

[40] Fang G, El Said B, Ivanov D, Hallett S. Smoothing artificial stress concentrations in voxel-based models of textile composites. Composites A 2016;80:270–84.

[41] Wintiba B, Vasiukov D, Panier S, Lomov S, Ehab Moustafa Kamel K, Massart T. Automated reconstruction and conformal discretization of 3D woven composite CT scans with local fiber volume fraction control. Compos Struct 2020;248:11238.

[42] Li A, Ehab Moustafa Kamel K, Wintiba B, Remmers J, Geers M, Massart T. A level set-based procedure for the cohesive modeling of yarn–yarn contacts in woven composite RVEs. Compos Struct 2023;304:116356.